Original Research Paper

IJES *Iranian Journal of Earth Sciences*
Vol. 14, No. 4, 2022, 285-300.
DOI: 10.30495/ijes.2021.685392

Application of mineral chemistry in determining magma fertility of the Tarom northern and southern intrusions, NW Iran

Narges Yasami[1], Majid Ghaderi[*1], Seyed Hedayatalah Mousavi Motlagh[1], Mir Ali Asghar Mokhtari[2]

1.Department of Economic Geology, Tarbiat Modares University, Tehran, Iran.
2.Department of Geology, Faculty of Sciences, University of Zanjan, Zanjan, Iran.

Received 12 February 2021; accepted 3 June 2021

Abstract

The Tarom metallogenic belt of the Alborz magmatic belt in NW Iran is characterized by two alignments of intrusion in its northern and southern parts. The northern intrusion is younger than the southern one. Mineral chemistry investigations on the northern and southern intrusions characterize calc-alkaline magmatism. The northern intrusion consists mostly of quartz monzonite, and the southern intrusion comprises 1) gabbro - pyroxene quartz monzodiorite – quartz monzodiorite series and quartz syenite; 2) gabbro-diorite. Electron microprobe chemistries indicate that the northern plagioclases are An22 to An49 (oligoclase to labradorite). Plagioclases from the southern intrusion are An35 to An54 (andesine to labradorite) and gabbro-diorite plagioclases are An65 to An61 (labradorite). All pyroxenes correspond to the Quad (diopside, augite, and clinoenstatite) and crystallized at <2 to 5 kbar and H_2O=10%. Formation temperatures of pyroxenes from the northern intrusion are in the range of 1100-1175°C. The northern feldspars show temperatures ~550°C. Formation temperatures for the clinopyroxene and feldspar from the southern intrusion are estimated at 1140-1185°C and 550-600°C, respectively. The Fe-rich biotite minerals from the northern intrusion suggest high oxygen fugacity magma. The northern and southern intrusions formed in an arc-related tectonic setting. The northern magma is sourced from the melting of a mixed mantle-crust in a subduction-related environment. The mineral composition of the northern intrusion implies magma fertility and porphyry mineralization which can be due to its high oxygen fugacity magma and lower crystallization pressure relative to those of the southern intrusion.

Keywords: *Mineral chemistry, thermobarometry, magma fertility, Alborz, Iran.*

1. Introduction

Mineralogical composition is one of the most effective parameters in classifying and describing intrusive rocks (Streckeisen 1976, Streckeisen and Le Maitre 1979, Pearce et al. 1984, Barbarin 1990). Evaluation of crystallization conditions and the processes influencing mineral crystallization could accurately explain the magmatic evolution of the host rocks. The chemical composition of clinopyroxene, amphibole, and biotite, represents valuable information, because they are present in different periods of crystallization of the host rock (Deer et al. 1992, Molina et al. 2009). Type and concentration of cations in various sites of general clinopyroxene formula can be used for specifying the magmatic series, tectono-magmatic setting, and evolution of host magma (Le Bas 1962, Leterrier et al. 1982, Morimoto et al. 1988, Beccaluva et al. 1989, Bindi et al. 1999, Avanzinelli et al. 2004). Depending on chemical composition and cation substitution in crystalline sites of clinopyroxene, conditions of crystallization (e.g., T, P, and fO_2) can be estimated (Schweitzer et al. 1979). Therefore, the formula for estimating the crystallization temperature of clinopyroxene has been developed (Taylor and Nimis 2000).

Moreover, phyllosilicate minerals (like biotite) are influenced by the chemistry of host magma (Beane 1974, 1974), and are used for determining magmatic series, oxygen fugacity, and crystallization temperature of magma.

This study gives information on the mineralogical and mineral chemical compositions of two different intrusions within a restricted area with the continental arc to post-collisional tectonic setting in the Cenozoic Tarom metallogenic belt (TMB) in western Alborz magmatic belt (AMB), NW Iran (Yasami et al. 2017, Mousavi Motlagh et al. 2019). These two intrusions are the northern Tarom intrusion and the southern Tarom intrusion (Fig 1a, b). Our study is focused on the mineral chemistry attributes of the northern (adjacent to Chodarchay high-sulfidation epithermal and porphyry mineralization) and the southern (adjacent to Chargar low-sulfidation epithermal mineralization) intrusions. Microprobe analyses on magmatic plagioclase, pyroxene, and biotite were performed to demonstrate the magmatic evolution of the northern and southern intrusions. This paper examines aspects of the porphyry mineralization potential of continental arc magmatic rocks that are exposed in the northern and southern Tarom, respectively, by mineral chemistry. The chemical composition of rock-forming minerals can be used to determine whether the differences in mineralization types

---

*Corresponding author.
E-mail address (es): mghaderi@modares.ac.ir

are related to the differences in mineral chemistry of the intrusions in the two parts (Yazdi et al. 2019).

2. Regional Geology

The Cenozoic Alborz magmatic belt (AMB) in northern Iran is a segment of the collisional Alpine–Himalayan orogenic belt extending from western Europe to Turkey, across Iran into western Afghanistan. This orogen formed through the African–Arabian plate and Eurasia convergence and the Tethys Ocean closure in the past 100 million years (Dabovski et al. 1991, Ricou et al. 1998, Axen et al. 2001). The Tethyan orogenic belt extends from the Alps, inward the Carpathians and Balkans, Taurids and Caucasus, Zagros, Makran, and, the Himalayas, to Indochina and into the southwest Pacific Ocean (Richards 2016).

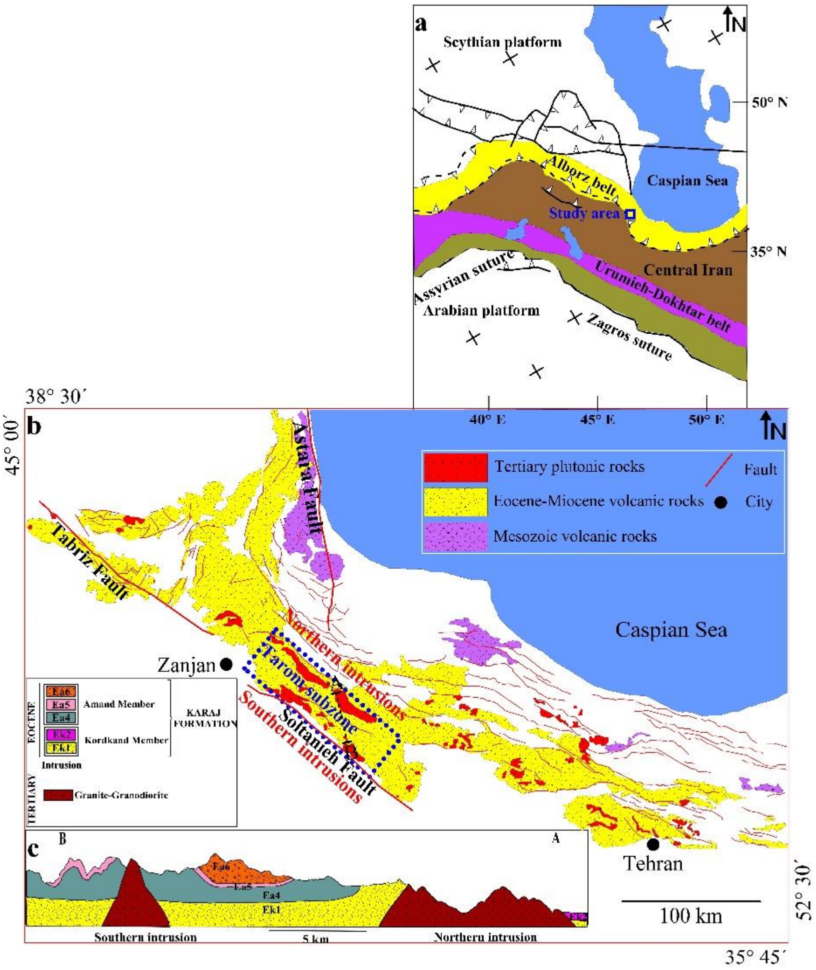

Fig 1. a) Location of the study area within the Tarom metallogenic belt of the Cenozoic Alborz magmatic belt (according to Rolland et al. 2009). b) Geological schematic map of the volcano-plutonic Tarom metallogenic belt in the western segment of the Alborz belt based on 1: 250,000 geological maps of Zanjan (revised after Hirayama et al. 1965, 1966) and Qazvin-Rasht (Annells et al. 1975). Tertiary intrusions and Karaj Formation are extended NW–SE. c) A geological cross-section from 1: 250,000 geological maps of Zanjan (revised after Hirayama et al. 1965, 1966) presenting the positions of the southern intrusions as well as the northern intrusions areas.

The TMB is situated in the western AMB in northwestern Iran. It is dominantly composed of Eocene volcanic, pyroclastic, and sedimentary strata intruded by late Eocene-Oligocene plutons. Eocene volcanism in the region began with mafic rocks, followed by intermediate and finished with felsic units. The volcanic units are mostly basalt, basaltic andesite, andesite, trachy-andesite, and dacite. The pyroclastics mainly show andesitic composition (Castro et al. 2013). Geochemically, the Eocene volcanic units are alkaline and high-Kcalc-alkaline (Castro et al. 2013). The alkaline units of usually potassic characteristics demonstrate shoshonitic signatures (Moinvaziri 1985, Asiabanha and Foden 2012). The plutonic rocks are mainly shallow intrusive bodies as dikes, sills, and stocks. In the western and central TMB, they show shoshonitic and high-K calc-alkaline affinities. In the western and eastern parts of the TMB, Oligocene volcanic units conceal the Eocene rocks. They are composed mainly of felsic lavas and pyroclastic deposits. The Neogene clastic red beds, indicating intra-mountain basins, reflect the AMB exhumation. Volcanic rocks, particularly of trachyte and dacite, are a significant constituent of the Neogene red beds in the northwest TMB (Castro et al. 2013).

3. Geology of the study area

The Tarom intrusions mainly outcrop as two series with NW trends in the north and south parts of Tarom (Fig 1). The LA-ICP–MS analyses of zircons give 35.7 ± 0.8 Ma to 37.7 ± 0.5 Ma as the crystallization ages of magmas for the northern intrusion (Nabatian et al. 2016). Magmatic rocks in the northern study area consist of two Eocene intrusions, and Eocene volcanic and volcaniclastic units (Fig 2a). Quartz monzonite to quartz syenite rocks intruded firstly at 38.34 ± 0.32 Ma, and then younger granite-alkali granite of 38.31 ± 0.31 Ma age was emplaced (Yasami 2018). It seems that the northern intrusion is connected to the extensional (normal) phase (Yasami et al. 2017). Large-ion lithophile elements (LILE) enrichment, high-field strength elements (HFSE) depletion, and clear positive Pb anomaly in the primitive mantle-normalized trace element patterns of the intrusions emphasize subduction-related arc magmatic characteristics. The intrusions originated in a volcanic arc to a post-collisional setting (Yasami et al. 2018; Sarem et al, 2021). The Eocene volcanic and volcaniclastic units in southern Tarom are composed of rhyolitic to basaltic strata (Fig 2b). Whole-rock geochemistry of the southern volcanic rocks shows calc-alkaline to high-K calc-alkaline to shoshonitic and metaluminous affinities (Mousavi Motlagh et al. 2019). The plutonic rocks intruded into the volcanic and volcaniclastic units. Intrusion outcrops are found in the two parts of this southern district (Fig 2b). The first outcropped intrusions include: (a) gabbro-pyroxene quartz monzodiorite - quartz monzodiorite series, and (b) quartz syenite. The pyroxene quartz monzodiorite body is intruded by quartz syenite.

The gabbro-diorite outcropped in the volcanic and volcaniclastic units as a second intrusion. The Zircon SHRIMP ages vary from 38.94 ±0.42 Ma to 38.32 ±0.17 Ma, and 37.78 ±0.28 Ma for the southern intrusion (Castro et al. 2013). The southern intrusion shows high-K calc-alkaline to shoshonitic affinity and is I-type and metaluminous. It was emplaced in a continental arc to a post-collisional tectonic setting (Mousavi Motlagh et al. 2019).

4. Methods

The sampling procedure involved the collection of 127 fresh rock samples from all intrusion outcrops. The samples were subjected to preparation in the laboratory at Tarbiat Modares University.

Fifty-six thin and 23 thin-polished sections were prepared. Electron Probe Micro Analysis (EPMA) was carried out on pyroxene (14 points), biotite (5 points), plagioclase (21 points), apatite (29 points), magnetite (5 points), chalcopyrite (5 points), and pyrite (7 points) on 13 thin and 5 thin-polished sections.

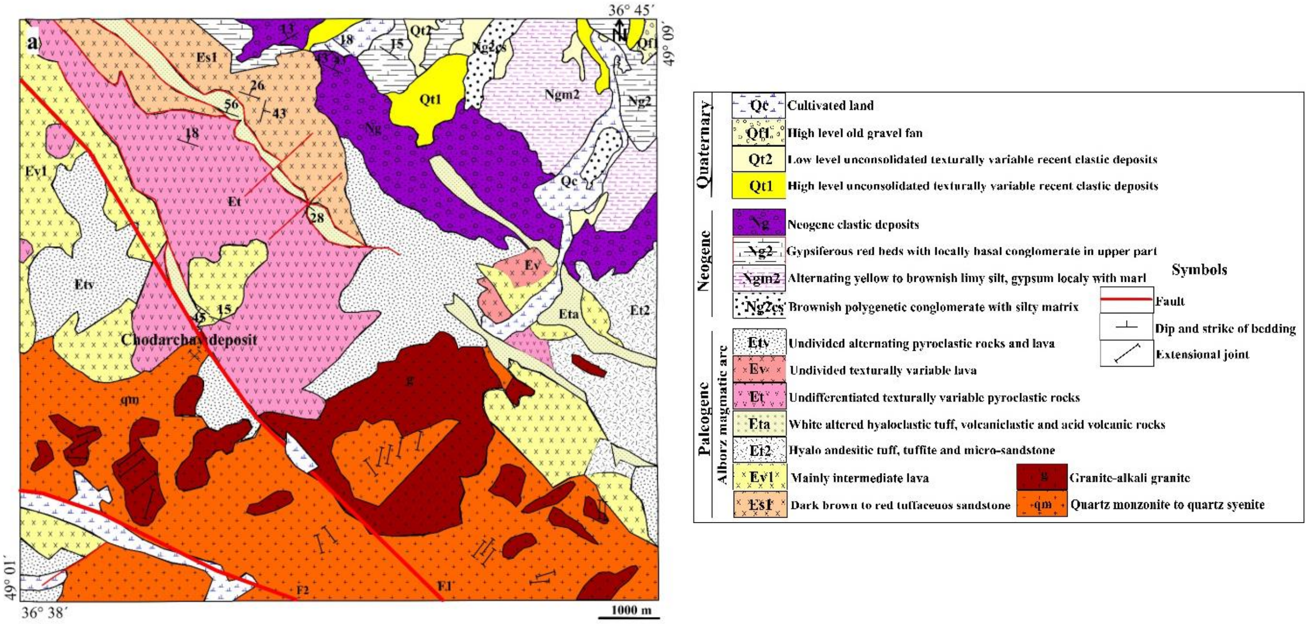

Fig 2. a) Distribution of igneous rocks in the study area according to the 1:100,000 geological map of Roudbar (revised after Nazari and Salamati 1998). The position of the Chodarchay deposit is displayed on the map.

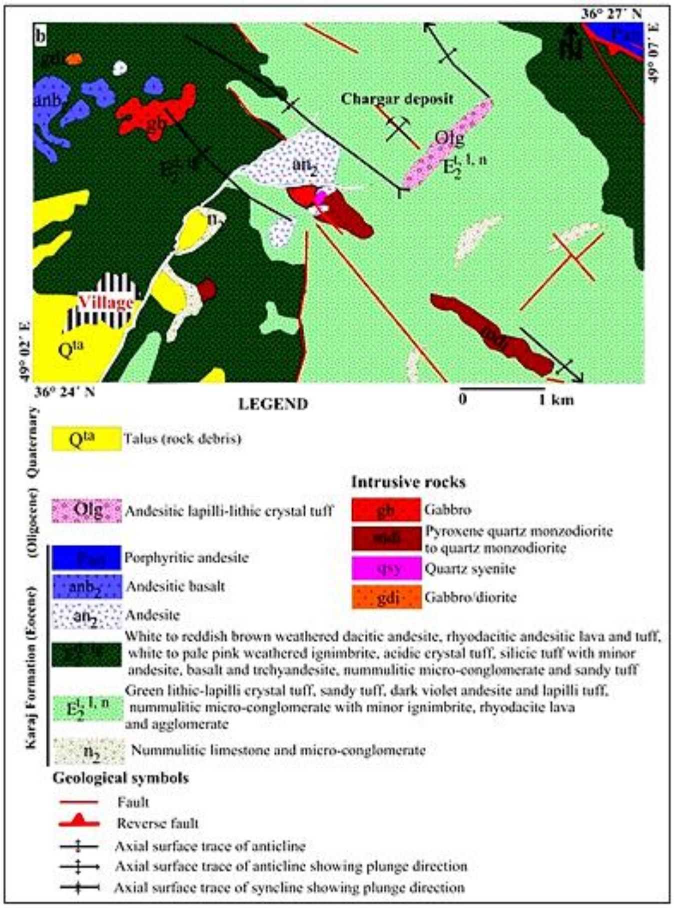

Fig 2. b) Geological map of the Chargar region (after Mousavi Motlagh and Ghaderi 2019). Based on Abhar 1:100,000 geological map (Revised by new field data after Hosseini et al. 2017).

The elemental analyses were performed using the CAMECA SX100 electron microprobe at the Iranian Mines and Mining Industries Development and Renovation Organization (IMIDRO) facility in Karaj, Iran. The probe operated at the acceleration voltage of 15kV, the probe current of 20nA with the beam diameter of 1-5 μm, ZAF correction, and 10 to 30 seconds counting time. Standard Name and Standard composition for electron microprobe analysis (EPMA) as follows (Table 1).

5. Results

5.1. Petrography of the northern intrusion

Quartz monzonite is the most abundant intrusion in the northern part of Tarom. The quartz monzonite is gray-colored and shows a joint system consisting of three intersecting joint sets (Fig 3a). A hand specimen of the quartz monzonite shows un-equigranular, and phaneritic textures (Fig 3b). Minerals consist of plagioclase, quartz, orthoclase, biotite, and amphibole.

Pyroxene occurs as a minor mineral. Zircon and apatite are common accessory minerals (Fig 3c, d). Orthoclase and perthite occur as subhedral crystals. Plagioclase grains are euhedral and show polysynthetic albite twinning. There are some plagioclase inclusions within the orthoclase crystals. Quartz crystals are anhedral grains and show undulatory extinction. Biotite and amphibole occur as subhedral minerals. Disseminated mineralization is observed in the quartz monzonite (Fig 3e, f).

Alkali granite-granite shows medium- to coarse-grained porphyritic and graphic textures. It consists of K-feldspar, plagioclase, quartz, and biotite. The accessory minerals include magnetite, titanite, apatite, and zircon. The alteration minerals are chlorite, iron oxide, clay minerals, and sericite.

5.2. Petrography of the southern intrusion

Gabbros make up the oldest part of the gabbro - pyroxene quartz monzodiorite - quartz monzodiorite series in southern Tarom. The gabbros consist of abundant euhedral and subhedral plagioclase and anhedral to subhedral clinopyroxene (Fig 4a). The gabbros have granular and somewhat intergranular textures. Spaces between plagioclase grains are occupied by clinopyroxene. Calcite and sericite have replaced plagioclase grains. Chlorite formed due to the alteration of clinopyroxene.

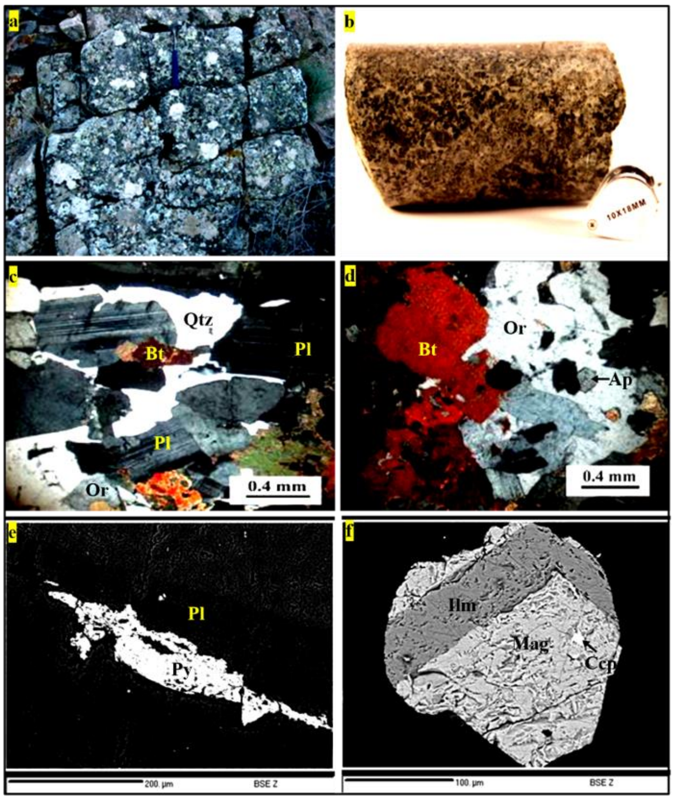

Fig 3. Images from the northern quartz monzonite intrusion. a) Field outcrop of quartz monzonite; b) Hand specimen of northern quartz monzonite (sample 24-7). c-d) Microscopic images in crossed polarized light. c) Biotite, plagioclase, orthoclase, and quartz. d) Biotite, orthoclase, and apatite. e-f) Backscattered electron images of sulfide mineralization in quartz monzonite. e) Pyrite occurrence within plagioclase. f) Chalcopyrite mineralization within magnetite. Abbreviations are from Kretz (1983). Pl: Plagioclase, Qtz: Quartz, Bt: Biotite, Or: Orthoclase, Ap: Apatite, Py: Pyrite, Mag: Magnetite, Ilm: Ilmenite, Ccp: Chalcopyrite.

Table 1. Standard name and standard composition for electron microprobe analysis

Standard Name	**Standard composition for electron microprobe analysis (EPMA)**
F On Flourite	Fluorite = Ca: 51.3341%, F: 48.6659%
Na On Albite	Albite = Na: 8.7671%
Mg On Perciclase	Periclase = Mg: 60.3028%
Al On Crundum	Corundum = Al: 52.9242%, O: 47.0758%
Si, Ca On Wollastonite	Wollastonite = Ca: 34.5026%, Si: 24.1772%, O: 41.3203%
K On Orthoclase	Orthoclase = K: 14.0472%, Al: 9.6939%, Si: 30.2715%, O: 45.9874% ,
Ti On Titanite	Titanite = Ti: 100.%
V On Vanadium	Vanadium = V: 100.%
Cr On Chromite	Chromite = Cr: 68.4195%, O: 31.5805%
Mn On Rhodonite	Rhodonite = O: 37.72%, Mg: 0.98%, Si: 21.63%, Ca: 5.2%, Mn: 33.68%, Fe: 0.79%
Fe On Specularite	Specularite = Fe: 69.94%, O: 30.06%
Standard error: 2%	

Pyroxene quartz monzodiorite with granular (at greater depth from drillings) to porphyritic textures is dark-colored and contains mainly clinopyroxene and plagioclase. Plagioclase is present as euhedral to subhedral tabular crystals and anhedral grains that show polysynthetic twins (Fig 4b, c). Quartz, alkali feldspar, plagioclase, and minor pyroxene (groundmass) are present as small crystals among other minerals (mainly clinopyroxene and plagioclase as phenocrysts). Sericitization, calcitization, and epidotization of plagioclase, and chloritization of pyroxene grains are observed. Magnetite is a minor constituent.

Quartz monzodiorite with granular texture is composed of plagioclase, amphibole, quartz, and alkali feldspar (Fig 4d, e). Clinopyroxene, apatite, and zircon are accessory minerals. Plagioclase occurs as subhedral crystals and shows polysynthetic twinning. Hornblende is seen as subhedral to anhedral crystals. Quartz grains are typically anhedral. K-feldspars have been crystallized as anhedral grains in the spaces among the minerals.

Quartz syenite exhibits granular texture and mainly contains orthoclase, plagioclase, quartz, and hornblende (Fig 4f). Clinopyroxene occurs as a minor mineral. Zircon forms the accessory phase. Alkalifeldspar is generally seen as subhedral to euhedral (tabular) crystals. Some alkali feldspar crystals formed at the plagioclase margins. Plagioclase occurs as subhedral to euhedral grains. Quartz is observed as anhedral grains and formed in the spaces between other crystals. Hornblende generally occurs as anhedral to subhedral crystals. Calcite and calcite-quartz veinlets crosscut these rocks. The gabbro-diorite is highly altered. These rocks exhibit granular texture and are composed predominantly of plagioclase, clinopyroxene, and hornblende (Fig 4g). Opaque minerals and sphene are common accessory minerals. Plagioclase occurs as subhedral to euhedral crystals. Hornblende crystals are mostly subhedral. Magnetite and clinopyroxene show a symplectic texture. Alteration to chlorite, calcite (Fig 4h), and clay minerals are observed. Disseminated ores including chalcopyrite, pyrite, galena, and bornite, occur in the gabbro-diorite (Fig 4i).

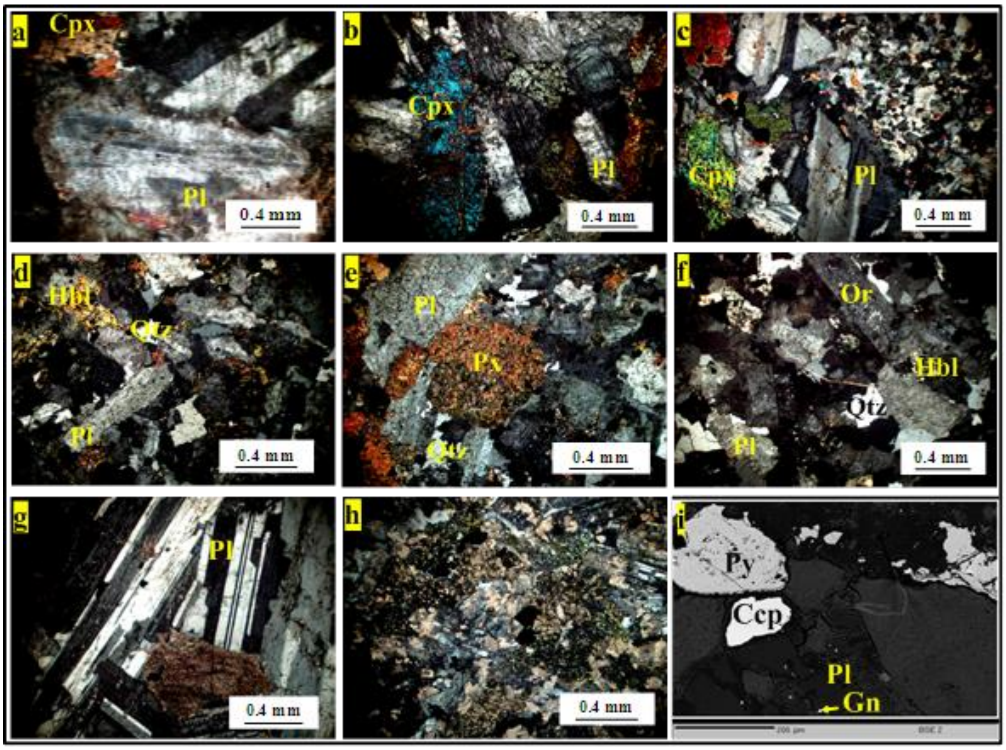

Fig 4. a) Clinopyroxene and plagioclase in the gabbro. b-c) Photomicrographs of pyroxene quartz monzodiorite in crossed polarized light. b) Clinopyroxene and plagioclase. c) Clinopyroxene and plagioclase accumulation beside fine-grained clinopyroxene and plagioclase. d-e) Photomicrographs of quartz monzodiorite in crossed polarized light. d) Plagioclase, hornblende, quartz, and K-feldspar. e) Subhedral crystal of pyroxene associated with quartz and plagioclase. f) Photomicrograph of quartz syenite in crossed polarized light; tabular alkali feldspar, quartz, hornblende, and plagioclase. g) Plagioclase and altered ferromagnesian mineral. h) Plagioclase replacement by calcite and hornblende altered to chlorite and opaque minerals. i) Backscattered electron images of sulfide mineralization in gabbro-diorite. Galena, chalcopyrite, and pyrite mineralization in gabbro-diorite. Abbreviations are from Kretz (1983). Cpx: Clinopyroxene, Pl: Plagioclase, Gn: Galena, Py: Pyrite, Ccp: Chalcopyrite.

5.3. Mineral chemistry

Table 2a displays representative EPMA data for the plagioclase phenocrysts from the northern and southern intrusions (Fig 5a-d). Different plagioclase grains from the northern intrusion present a range of compositions from An_{22} to An_{49} (oligoclase to labradorite). Various plagioclase crystals from the southern intrusion series show a range of composition from An_{35} to An_{54} (andesine to labradorite) and plagioclases from the southern gabbro-diorite show a composition of An_{56} to An_{61} (labradorite) (Fig 5e). Table 2b displays representative EPMA data of the pyroxene crystals from the northern and southern intrusions (Fig 5f-i). Compositional ranges of the pyroxenes are displayed in Fig 5, where the composition is normalized to Ca+Mg+Fe=100 in which $Fe=Fe^{2+}+Fe^{3+}+Mn^{2+}$.

Based on the EPMA data, all of the pyroxenes are plotted within the Quad field in the Q-J diagram. They all correspond to the Quad (Fig 5j) pyroxenes (mainly augite, Fig 5k). The classification of Nachit et al. (2005) for the analyzed biotites in the northern intrusion implies a magmatic origin (Fig 5l). TiO_2 ranges from 4.06 to 4.65 *wt.%* in these crystals (Table 2c). Apatite is one of the most common accessory minerals in many rock types. Table 2d displays representative EPMA data for apatites from the southern intrusion series (Fig 6a, b). The P_2O_5 contents vary from 36.78 to 44.35 *wt.%*, while CaO varies between 48.18 and 54 *wt.%*. FeOT contents of the apatites are low (<1 *wt.%;* except one sample).

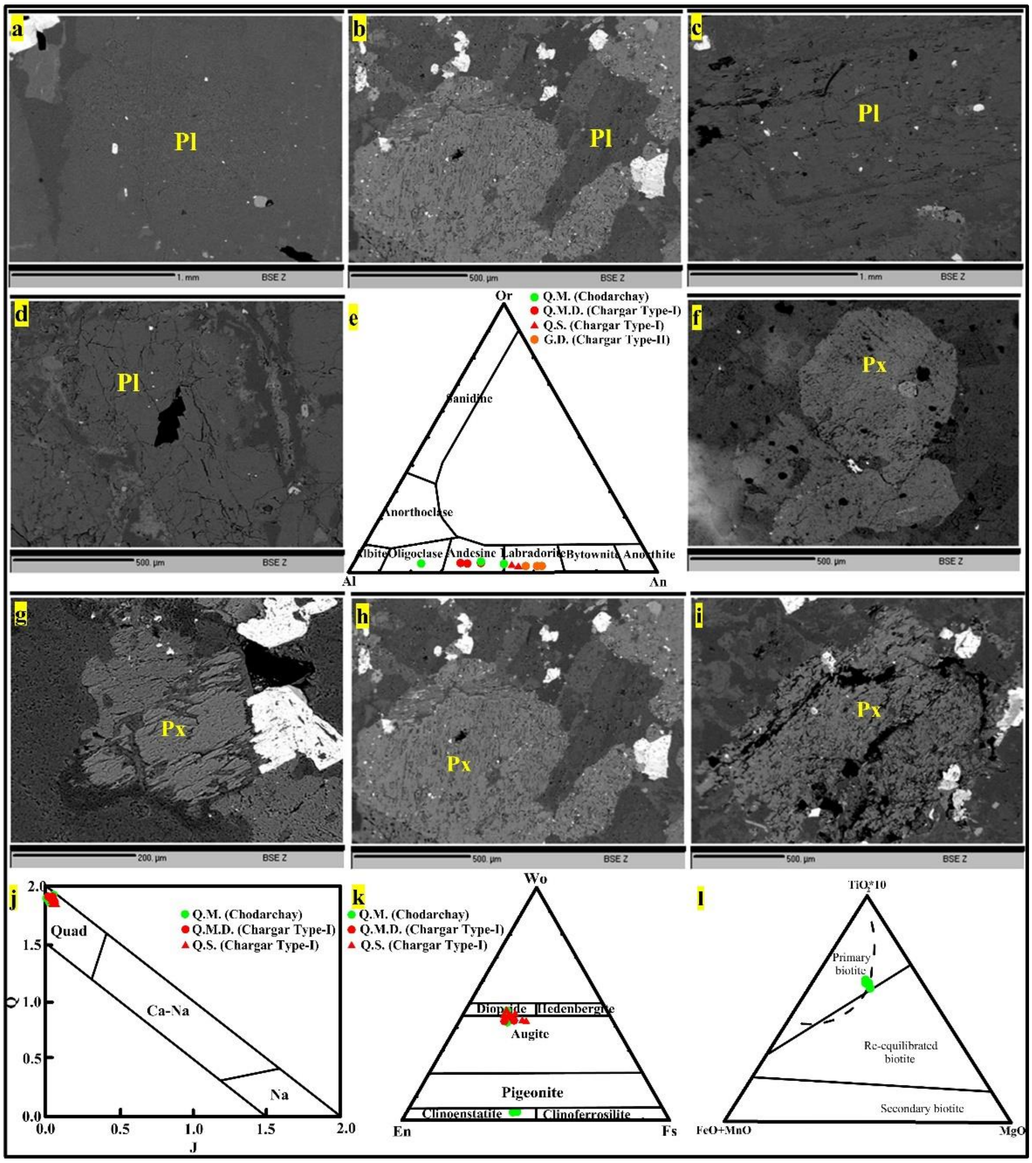

Fig 5. a-d) Back-scattered EPMA images of plagioclase from a) The northern quartz monzonite (sample 24.7). b) The southern quartz monzodiorite (sample 107). c) The southern quartz syenite (sample 108). d) Gabbro-diorite (sample 117). e) A plot of the northern and southern plagioclase compositions on the feldspar ternary diagram (Deer et al. 1992). The northern plagioclases present a range of composition from An22 to An49 (oligoclase to labradorite), the southern intrusion series plagioclases show a range of composition from An35 to An54 (andesine to labradorite) and the southern gabbro-diorite plagioclases show a composition of An56 to An61 (labradorite). Back-scattered electron images of pyroxene from f-g) Northern quartz monzonite (sample 24.7). h) Southern quartz monzodiorite (sample 107). i) Southern quartz syenite (sample 108). j) The plot of northern and southern pyroxene compositions in the Q-J classification diagram (Morimoto et al. 1988). They all correspond to the Quad; k) Wo–En–Fs triangle diagram for pyroxene classification (Morimoto et al. 1988); l) TiO2*10-Fe+MnO-MgO triangular diagram for biotites from the northern intrusion (Nachit et al. 2005). Biotites in the northern intrusion imply a magmatic origin. Mineral abbreviations are from Kretz (1983). Pl: Plagioclase, Px: Pyroxene.

On the Ca/100-Mn*100-Fe*100 triangular diagram, different apatite grains from the southern intrusion plot between Ca/100 and Fe*100 corners (Fig 6c). According to Fe-Mn-Ca*100 and Na-Mn-Ca*100 triangular diagrams (Fig 6d, e), the apatites plot in the overlapping field of the low-temperature hydrothermal system, the mafic system, and the system unrelated to intermediate–mafic rocks, as defined by Piccoli and Candela (2002), with outliers in the latter and the hydrothermal systems. Some apatite grains are altered by a low-temperature hydrothermal system and these apatite minerals are not considered to have a magmatic origin. However, almost all concentrations plot in the mafic system (Fig 6d).

Table 2. a) EPMA data for plagioclase (in *wt.%*) from the northern and southern intrusions. b) EPMA data of pyroxene (in *wt.%*) from the northern and southern Quartz monzodiorite and Quartz syenite intrusions. c) EPMA data for biotites (in *wt.%*) from the northern intrusion. d) Representative EPMA data (in *wt.%*) for apatites from the southern intrusion series. R.U.: Rock unit; Q.M.: Quartz monzonite; Q.M.D.: Quartz monzodiorite; G.D.: Gabbro-diorite; Q.S: Quartz syenite; G.: Gabbro.

a)	**R.U.**	**SiO_2**	**TiO_2**	**Al_2O_3**	**Cr_2O_3**	**FeOT**	**MnO**	**MgO**	**CaO**	**Na_2O**	**K_2O**	**V_2O_3**	**Ga_2O_3**	**Total**
Northern	Q.M.	53.43	0.11	29.09	0	0.29	0	0.04	10.73	5.89	0.41	0.02	0	100.01
Northern	Q.M.	59.36	0.04	26.45	0.01	0.35	0	0.02	8.01	5.93	0.46	0	0.07	100.7
Northern	Q.M.	62.64	0.02	23.12	0	0.22	0	0.01	4.62	8.53	0.34	0	0.09	99.59
Northern	Q.M	62.35	0.03	22.96	0	0.36	0	0.01	4.72	8.61	0.61	0	0	100.1
Northern	Q.M	57.33	0.03	25.84	0	0.39	0	0.02	8.08	6.10	0.49	0	0	98.9
Southern	Q.M.D.	58.61	0.03	25.89	0	0.42	0	0.01	7.73	6.97	0.59	0.01	0	100.23
Southern	Q.M.D.	60.45	0.03	25.2	0.01	0.43	0	0.02	7.97	6.04	0.49	0	0	100.64
Southern	Q.M.D.	58.85	0.04	26.13	0	0.53	0	0	7.32	7.27	0.55	0	0	100.69
Southern	Q.M.D.	58.83	0.04	27.02	0	0.61	0	0.01	7.28	6.62	0.58	0	0	99.1
Southern	Q.M.D.	58.68	0.03	24.99	0	0.59	0	0.01	7.07	6.78	0.60	0	0	99
Southern	Q.S.	54.07	0.07	30.09	0.02	0.35	0	0.02	10.27	4.64	0.41	0	0	99.94
Southern	Q.S.	55.21	0.05	29.65	0.02	0.34	0.01	0.03	8.52	6.28	0.51	0	0	100.62
Southern	Q.S.	54.99	0.05	28.9	0	0.4	0	0	9.73	4.82	0.46	0	0	99.35
Southern	Q.S.	54.54	0.05	27.49	0	0.48	0	0.01	10.29	5.30	0.38	0	0	100.1
Southern	Q.S.	54.93	0.06	27.34	0.01	0.6	0	0	9.96	5.23	0.31	0	0	99.83
Southern	G.D.	51.08	0.11	30.86	0.02	0.81	0.01	0.05	12.47	4.38	0.37	0.01	0.02	100.19
Southern	G.D.	50.35	0.1	31.08	0	0.95	0.03	0.04	13.12	4.3	0.35	0.02	0	100.34
Southern	G.D.	53.62	0.1	29.16	0.01	0.93	0	0.05	11.58	4.77	0.39	0	0	100.63
Southern	G.D.	53.21	0.1	28.74	0.01	0.66	0.01	0.05	11.69	4.63	0.22	0	0	99.9
Southern	G.D.	52.55	0.09	29.15	0	0.85	0. 02	0.05	12.09	4.16	0.35	0.01	0	100.1
Southern	G.D.	52.89	0.1	29.14	0	0.68	0	0.04	11.67	4.32	0.55	0	0.01	99.89

b)	**R.U.**	**SiO_2**	**TiO_2**	**Al_2O_3**	**Cr_2O_3**	**FeOT**	**MnO**	**MgO**	**CaO**	**Na_2O**	**K_2O**	**V_2O_3**	**Total**
Northern	Q.M.	53.57	0.47	1.32	0	10.72	0.52	13.58	20	0.24	0	0.06	100.48
Northern	Q.M.	52.92	0.4	1.29	0	9.09	0.53	12.96	21.3	0.38	0.04	0.04	98.95
Northern	Q.M.	52.64	0.24	1.24	0	9.7	0.52	12.97	22.56	0.28	0.02	0.02	100.19
Northern	Q.M.	52.94	0.22	0.43	0	24.1	1.02	18.63	1.33	0	0.01	0.02	98.7
Northern	Q.M.	53.66	0.13	0.43	0	22.96	1.02	18.7	1.53	0.06	0.01	0	98.5
Southern	Q.M.D.	53.19	0.2	1.32	0.06	10.26	0.34	13.41	21.02	0.15	0	0	99.95
Southern	Q.M.D.	52.5	0.23	0.7	0	11.86	0.49	12.5	20.19	0.18	0	0	98.65
Southern	Q.M.D.	53.87	0.08	0.73	0.01	8.72	0.55	12.91	22.39	0.24	0.01	0	99.51
Southern	Q.S.	52.51	0.15	1.7	0.02	9.37	0.49	13.5	22.04	0.32	0	0	100.1
Southern	Q.S.	51.74	0.27	2.79	0.03	11.15	0.34	11.78	20.74	0.31	0.01	0	99.16
Southern	Q.S.	49.13	1.39	6.48	0.01	11.7	0.26	14.84	10.53	2.48	0.91	0.13	97.86
Southern	Q.S.	52.59	0.27	2.81	0	9.56	0.41	13.6	21.05	0.25	0.01	0.03	100.58
Southern	Q.S.	51.84	0.14	2.45	0	13.17	0.59	11.21	19.7	0.42	0.01	0	99.53
Southern	Q.S.	51.17	0.22	2.67	0	14.09	0.82	11.32	20.2	0.33	0.01	0	100.83

c)	**R.U.**	**SiO_2**	**TiO_2**	**Al_2O_3**	**Cr_2O_3**	**FeOT**	**MnO**	**MgO**	**CaO**	**Na_2O**	**K_2O**	**V_2O_3**	**Total**
Northern	Q.M.	39.28	4.65	12.2	0.01	14.23	0.14	14.12	0.02	0.24	9.97	0.25	95.11
Northern	Q.M.	40.47	4.06	12.81	0.01	13.51	0.14	15.63	0.02	0.28	10.43	0.16	97.52
Northern	Q.M.	39.88	4.34	12.6	0.01	13.86	0.14	14.88	0.02	0.27	10.11	0.19	96.30
Northern	Q.M.	39.59	4.48	12.31	0.01	14.05	0.14	14.59	0.02	0.25	10.04	0.21	95.69
Northern	Q.M.	40.17	4.41	12.59	0.01	13.67	0.14	15.25	0.02	0.27	10.28	0.18	97.01

Table 2. Continued

d)	R.U.	SiO_2	TiO_2	Al_2O_3	FeOT	MnO	MgO	CaO	Na_2O	K_2O	Ga_2O_3	Y_2O_3	Ce_2O_3	Nd_2O_3	SO_2	P_2O_5	Total
Southern	Q.M.D.	0.1	0	0.1	0.64	0.11	0.29	51.88	0.01	0.13	0	0.18	0	2.89	0	42.73	99.06
Southern	Q.M.D.	0.07	0	0.08	1.41	0.04	0.01	50.04	0.12	0.03	0	0.06	0	2.38	0	44.35	98.64
Southern	Q.M.D.	0.51	0	0.24	0.11	0.08	0.04	48.18	0.03	0.06	0	0.24	0	3.99	0	36.78	90.26
Southern	Q.M.D.	0.54	0	0.37	0.11	0.06	0.03	49.01	0.05	0.04	0	0.4	0	3.7	0.05	36.9	91.26
Southern	Q.M.D.	0.91	0.17	0.42	0.54	0.05	0.24	51.2	0.06	0.01	0	0.27	0.4	3.85	0.09	39.56	97.77
Southern	Q.S.	0.4	0.02	0.17	0.18	0.08	0.05	52.53	0.26	0.01	0	0.41	0	2.73	0	43.91	100.8
Southern	Q.S.	0.44	0.07	0.16	0.43	0.07	0.04	51.55	0.25	0.02	0.05	0.39	0	3.24	0.05	41.91	98.67
Southern	Q.S.	0.5	0.08	0.41	0.32	0.04	0.01	52.01	0.27	0.01	0	0.26	0.43	2.8	0.07	42.48	99.69
Southern	Q.S.	0.29	0.58	0.57	0.76	0.04	0.37	49.01	0.09	0.02	0	0.44	0	2.06	0.07	43.85	98.15
Southern	Q.S.	0	0.01	0.03	0.7	0.07	0.05	52.06	0.25	0	0.09	0.38	0	1.99	0	43.09	98.72
Southern	Q.S.	0.53	0.04	0.49	0.83	0.1	0.19	50.24	0.09	0.06	0	0.33	0	2.86	0.08	43.19	99.03
Southern	G.	1.7	0	0.61	0.69	0.33	0.1	50.29	0.35	0	0	0.21	0	2.93	0.32	42.62	100.15
Southern	G.	0.56	0	0.3	0.22	0.07	0.05	53.11	0.27	0.08	0	0.22	0	1.39	0.14	42.41	98.82
Southern	G.	0.88	0	0.27	0.46	0.04	0.23	52.68	0.12	0.12	0	0.09	0	1.99	0.16	42.85	99.89
Southern	G.	0.42	0	0	0.24	0.11	0	52.37	0.17	0	0	0.28	1.08	1.74	0.05	42.31	98.77
Southern	G.	0.32	0	0.1	0.21	0.08	0	52.68	0.15	0	0	0.18	0	1.88	0.04	42.67	98.31
Southern	G.	0.35	0	0.63	0.32	0.09	0	52.96	0.14	0	0	0.19	0	1.87	0.05	42.35	98.95
Southern	G.	0.41	0	0.46	0.42	0.04	0.05	53.52	0.1	0	0	0.17	0	1.83	0.09	42.82	99.91
Southern	G.	0.07	0	0	0.16	0.06	0.01	52.67	0.1	0	0.05	0.15	2.66	0.44	0	42.58	98.95
Southern	G.	0.01	0	0	0.17	0.06	0.02	53.18	0.13	0	0.07	0.2	1.82	0.44	0	42.61	98.71
Southern	G.	0.33	0	0.28	0.18	0.08	0.04	53.82	0.17	0	0.1	0.05	0	1.57	0.05	42.57	99.24
Southern	G.	0.38	0	0.04	0.16	0.07	0	54	0.11	0	0	0	0	2.08	0.09	42.78	99.71
Southern	Q.S.	0.46	0	0.37	0.18	0.05	0.04	52.19	0.08	0.05	-	0.37	0	1.37	0.16	42.06	97.41
Southern	Q.S.	0.44	0.04	0	0.25	0.09	0.02	52.2	0.09	0.04	-	0.11	0	1.17	0.13	43.02	97.6
Southern	Q.S.	0.43	0	0.74	0.24	0.08	0.04	52.14	0.07	0.04	-	0.36	0.51	2.02	0.13	42.39	99.19
Southern	Q.S.	0.35	0	0.02	0.15	0.07	0.03	53.22	0.19	0.03	-	0.23	0	1.56	0.1	42.82	98.79
Southern	Q.S.	0.29	0	0.66	0.25	0.09	0.03	52.27	0	0.06	-	0.27	0	1.52	0.18	42.91	98.54
Southern	Q.S.	0.37	0	0	0.06	0.1	0.02	53.27	0.04	0	-	0.23	0	1.78	0.17	42.32	98.36
Southern	Q.S.	0.3	0	0	0.13	0.07	0.03	52.78	0.09	0	-	0.16	0.97	1.44	0.2	42.49	98.66

Table 3a displays representative EPMA results for magnetites from the southern intrusion (Fig 6f, g). The EPMA data show the magnetites to be slightly titaniferous. Pyrite occurs as a disseminated phase within the northern quartz monzonite and southern gabbro-diorite (Figs. 3e, 4i). Due to the crystal structure of pyrite, trace elements present in the hydrothermal fluid can be incorporated into the chemistry of pyrite grains (Deol et al. 2012). Table 3b shows the EPMA results for the composition of the pyrites within the northern and southern intrusions. These analyses enabled us to identify geochemical trends, trace element signatures changing in minerals, and possibly differentiates between two genetically different types of pyrite to understand ore-forming processes. Chalcopyrite was observed within the northern quartz monzonite and southern gabbro-diorite (Figs. 3f, 4i). The EPMA data of the chalcopyrite within the southern gabbro-diorite intrusion are presented in Table 3c.

Table 3. a) EPMA results (in *wt.%*) of magnetite from the northern intrusion. b) Representative EPMA data (in *wt.%*) for pyrites from the northern (quartz monzonite) and southern (gabbro-diorite) intrusions. c) Representative EPMA analytical results (in *wt.%*) for the chalcopyrite crystals from the southern gabbro-diorite intrusion. Q.M.: Quartz monzonite; G.D.: Gabbro-diorite.

a)

TiO_2	Al_2O_3	FeO	MnO	CaO	V_2O_3	Total
0.52	0.21	87.29	0.01	0.02	0.59	89.4
0.31	0.98	88.65	0	0.07	0	91.81
0.51	0.25	87.34	0	0.05	0.39	92.37
0.34	1	88.61	0	0.04	0.09	91.84
0.29	0.99	88.7	0	0.07	0.02	91.64

b)

	Fe	Ti	S	Cu	Ga	As	Se	Sn	Hg	Pb	Bi	Zn	Te	Ge	Total
Northern (Q.M.)	44.88	0	52.93	0.09	0	1	0.02	-	0	0.3	0.13	0.36	0	0.03	99.74
Northern (Q.M)	43.86	0.02	52.72	0.33	0	0.86	0	-	0.07	0.24	0.17	0	0	0.05	98.32

	Fe	Ti	S	Cu	Ga	As	Se	Sn	Hg	Pb	Bi	Zn	Te	Ge	Total
Southern (G.D.)	45.5	-	53.17	0	0	0.01	-	0.05	0.02	0.17	0.16	0	0	0.06	99.15
Southern (G.D.)	44.47	-	53.92	0.08	0.05	0.06	-	0	0.11	0.22	0.23	0	0.02	0.01	99.19
Southern (G.D.)	45.37	-	54.56	0	0.06	0.05	-	0	0	0.22	0.24	0.06	0.01	0	100.57
Southern (G.D.)	45.32	-	52.98	0.07	0.01	0.08	-	0	0	0.31	0.18	0	0	0	98.99
Southern (G.D.)	45.69	-	53.72	0	0.04	0.08	-	0.02	0.02	0.22	0.24	0.03	0.01	0.07	100.15

c)

	Fe	Cu	S	Sn	Mn	Ag	As	Hg	Bi	Te	Ga	Ge	Mn	Pb	Zn	Total
Southern (G.D.)	30.04	34.40	33.95	0.01	0.00	0.00	0.00	0.00	0.09	0.00	0.03	0.00	0.00	0.11	0.00	98.63
Southern (G.D.)	29.79	34.72	34.61	0.03	0.02	0.00	0.01	0.04	0.09	0.00	0.01	0.00	0.02	0.10	0.00	99.44
Southern (G.D.)	29.83	34.79	34.04	0.04	0.00	0.00	0.00	0.00	0.14	0.00	0.02	0.03	0.00	0.00	0.05	98.94
Southern (G.D.)	29.53	34.87	34.28	0.02	0.01	0.00	0.00	0.03	0.12	0.00	0.00	0.00	0.01	0.21	0.01	99.09
Southern (G.D.)	29.67	34.94	34.45	0.03	0.00	0.00	0.00	0.00	0.11	0.03	0.00	0.00	0.00	0.31	0.00	99.54

6. Discussion

6.1. Magmatic series

Some researchers have investigated the chemistry of biotites and clinopyroxenes for estimating magma types and their primary tectonic settings (e.g., Kushiro 1960, Le Bas 1962, Nisbet and Pearce 1977, Pearce et al. 1984, Abdel Rahman1994). Biotite minerals from I-type intrusions are comparatively Mg-enriched, whereas biotites in S-type intrusions show relative Al enrichment (Abdel Rahman 1994). Magnesian biotites from the northern intrusion also affirm an I-type classification for this intrusion. Using biotite compositions, Abdel Rahman (1994) indicated that MgO vs. Al_2O_3 diagram can help to distinguish between three compositionally separate fields (Fig 7a): (A) orogenic alkaline suites associated with extensional tectonic settings, (P) peraluminous suites, involving collisional S-type granites, and (C) calc-alkaline orogenic suites, involving I-type suites, constituted within the subduction-related setting. All of the biotites from the Tarom northern intrusion fall on the calc-alkaline fields. Based on biotite composition and FeO/(FeO+MgO) vs. MgO diagram (Zhou 1986), the source material of the intrusions can be distinguished. According to the mentioned diagram, biotites from the northern intrusion place on the crust-mantle mixing field (Fig 7b).

The chemical composition and tectonic environment of the host magma intensely affect pyroxene composition. This fact is widely used for the determination of magma series, and the geological setting of basic rocks (Kushiro 1960, Schweitzer et al. 1979, Hout et al. 2002). In clinopyroxene crystals, Ca, Ti, Al, and Na show high-frequency concentration in the crystal formula and the degree of magma alkalinity can be determined using these elements (Le Bas 1962, Leterrier et al. 1982). In Al_2O_3 vs. SiO_2 diagram (Le Bas 1962); all samples are placed in the sub-alkaline field (Fig 7c).

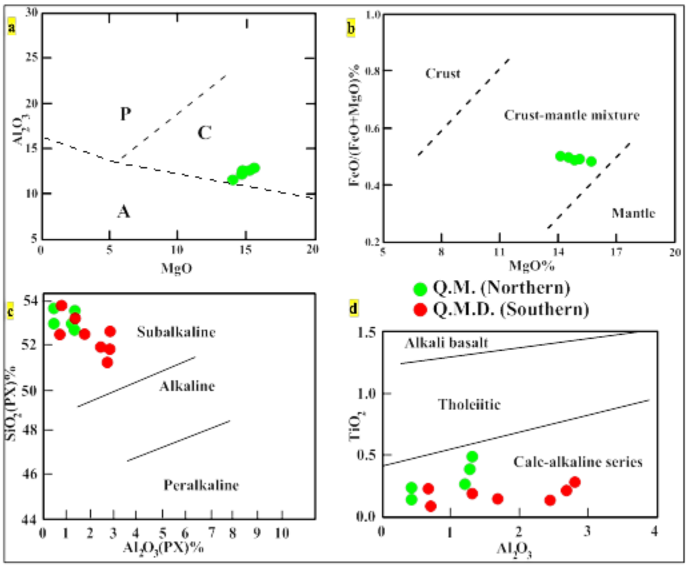

Fig 7. a) Location of the biotite compositions from the northern intrusion on the MgO vs. Al_2O_3 diagram (Abdel Rahman 1994). A: Anorogenic alkaline suites formed in conjunction with extensional tectonic settings, P: Peraluminous suites, including collisional S-type granites, C: Calc-alkaline orogenic, including the I-type, suites formed within subduction-related settings. b) Biotite minerals from the northern quartz monzonite on the MgO vs. FeO/(FeO+MgO) diagram (Zhou 1986) plot within the mantle-crust mixing source area. c) SiO_2 vs. Al_2O_3 diagram (Le Bas 1962) for pyroxenes of the northern and southern intrusions which plot within the sub-alkaline field. d) TiO_2 vs. Al_2O_3 diagram according to clinopyroxene compositions (Le Bas 1962) for the northern and southern intrusions which plot in the calc-alkaline field.

Furthermore, if physical conditions are similar, magma types can be illustrated using the Al_2O_3–TiO_2 diagram. The pyroxenes from the northern and southern intrusions are placed into the calc-alkaline series, showing their formation within a subduction-related setting (Fig7d).

6.2. Oxygen fugacity

Oxygen fugacity has significant effects on the liquidus temperature, controlling magmatic processes on melt and crystal compositions, crystallization succession, and crystallized mineral types (Kilinc et al. 1983, Botcharnikov et al. 2005, Moretti 2005, France et al. 2010). The Fe and Mg contents in biotite depend on oxygen fugacity during the magma cooling process (Wones and Eugster 1965). In high fO_2 conditions, biotite crystals are Fe-rich and magnetite coexists with biotite, while in low fO_2 crystallization conditions, biotite will be poor in Fe and magnetite rarely exists (Castro and Stephen 1992). Biotite minerals from the northern intrusion show high contents of MgO (14.12-15.63%) and FeO (13.51-14.23%) (Table 2c), which implies their formation in a high oxygen fugacity condition. The existence of opaque minerals such as magnetite confirms the high oxygen fugacity of the magma. Fe^{3+} content in pyroxenes is related to the Al^{VI} content, which indicates that it hinges on the Al balance in tetrahedral and octahedral positions (France et al. 2010). In all clinopyroxenes from the northern and southern intrusions, the Al atom in the T site is enough for filling the absence of Si^{4+} in the tetrahedral sites (Fig 8a).

Environments of high oxygen fugacity are expected for the mineralization of economic metals (Wyborn and Sun 1994, Sun et al. 2004). Therefore, crystallized intrusions in high oxygen fugacity environments should be accounted for potential mineralization. In the Tarom northern intrusion, these are host rocks for some base metal mineralization such as Lubin-Zardeh (Zamanian et al. 2019) and Chodarchay (Yasami et al. 2017) areas.

6.3. Thermobarometry

The clinopyroxene Al content at high- and low-pressure is related to the $NaAlSi_3O_8$=$NaAlSi_2O_6$+SiO_2 and $CaAl_2Si_2O_6$=$CaAl_2SiO_6$+SiO_2 reactions, respectively (Green and Ringwood 1967). The first and second reactions occur at depths of ~120 *km*, and <40 *km*. Aluminum content in the pyroxene structure is utilized for determining the depth of the magma reservoir. Helz (1976) has shown the importance of Al distribution in the octahedral positions of clinopyroxene as a favorable criterion to assess the magma water content and the formation pressure of magmatic units. Based on this model, pyroxenes of the northern (quartz monzonite) and southern (quartz monzodiorite and quartz syenite) intrusions plot at a 5 *kbar* pressure and H_2O=10% fields. The Al^{VI} amounts in clinopyroxene crystals are less than 0.1 so these minerals have been crystallized at < 5 *kbar* (Helz 1976). However, according to the position of the samples relative to the boundaries of this diagram, it seems that the northern intrusion crystallized at a lower pressure and a higher H_2O content (Fig 8b). The Al^{VI}/Al^{IV}, $Ti+Al^{IV}/Si$, and $TiO_2/(Mg/Mg+Fe)$ ratios in pyroxene could act as a pressure criterion. In the Al^{VI} vs. Al^{IV} diagram (Aoki and Shiba 1973), pyroxenes from the northern and southern intrusions place in a moderate range of pressure (Fig 8c). According to the XPT vs. YPT diagram (Soesoo 1997), the formation pressure of clinopyroxene from the northern and southern intrusions are <2 to 5 kbar (Fig 8d).

Pyroxene minerals show a temperature range of 1140 to 1185°*C* for the southern intrusion series (Fig 8e). The temperatures of pyroxenes from the northern intrusion are between 1100 and 1175°*C*. Plagioclase is found in almost every type of rock, but its composition and abundance depend on the rock type, which makes plagioclase useful; e.g., in igneous rock analysis (Helgadottir 2016). Its composition is very reactive to temperature, pressure, and water content in a melt (Helgadottir 2016).

The composition of feldspars in the northern and southern intrusions on the ternary feldspar system implies temperatures ~550°*C* and range from 550 to 600°*C*, respectively (Fig 8f). The reason for the low temperature of feldspars formation can be due to the transformation of sub-solidus during the cooling of the intrusions (Kroll et al. 1993, Anderson 1996).

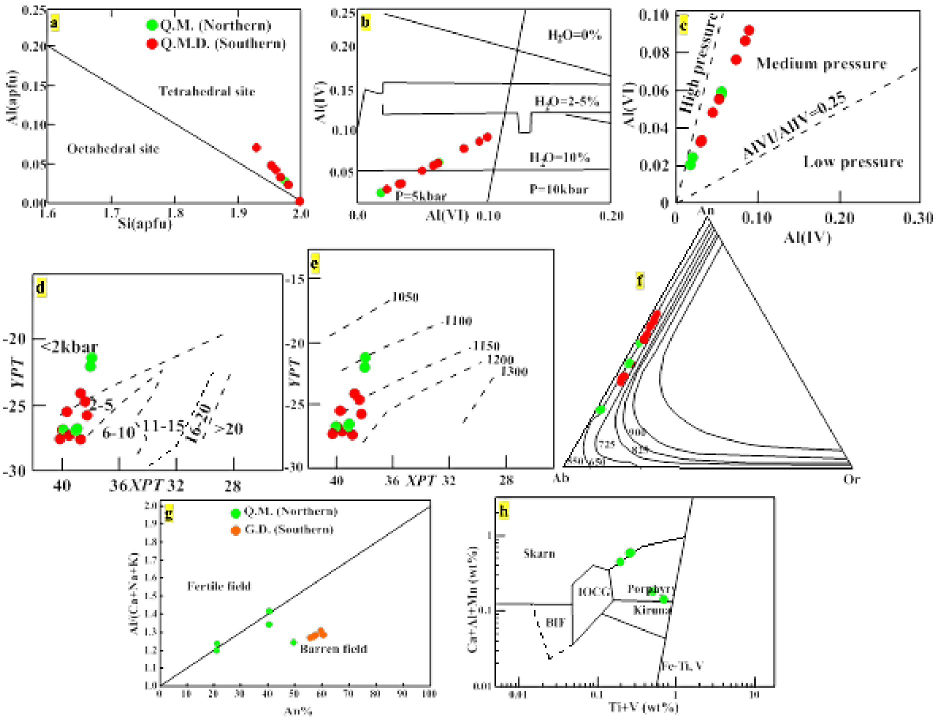

Fig 8. a) Si (a.p.f.u) versus Al (a.p.f.u) plot (after Leterrier et al. 1982) shows all pyroxenes from the northern and southern intrusions with shares of Al in the tetrahedral sites. b) Al^{VI} vs. Al^{IV} diagram (Aoki and Shiba 1973) for pressure assessment based on the clinopyroxene compositions from the northern and southern intrusions. The water content of magma for these intrusions was about 10%. c) Al^{VI} vs. Al^{IV} diagram (Heltz 1976) for northern and southern pyroxenes. d) Determination of clinopyroxene formation pressure using XPT vs. YPT diagram (Soesoo 1997). e) Determination of pyroxene temperature using XPT vs. YPT diagram (Soesoo 1997). Temperatures range from 1140 to 1185°*C* for the southern quartz monzodiorite pyroxenes. The higher temperature of northern pyroxenes is 1175°*C*. The lower temperature of northern clinopyroxene is 1100°*C*. f) The plot of feldspar compositions from the southern and northern intrusions on the ternary Ab-An-Or diagram (Seck 1971). g) Magmatic plagioclase compositions from the northern quartz monzonite and southern gabbro-diorite. h) Ca+Al+Mn vs. Ti+V discriminant diagram (Borderlines from Dupuis and Beaudoin 2011) for compositions of magnetite in northern intrusions.

6.4. Fertility of magmas

Magmatic plagioclases occur plentifully as phenocryst and groundmass crystals in porphyry type mineralization-related intrusions (Seedorff et al. 2005) and are used as an indicator mineral for porphyry type Cu-Mo mineralization (Cooke et al. 2017). Magmatic plagioclase from the Earth's largest porphyry Cu-Mo region had higher Al abundances than typical arc magmas of the Caribbean porphyry unrelated deposits. The high magmatic water contents can explain the excess Al in plagioclase (Williamson et al. 2016). One essential prerequisite for porphyry ore formation is the higher H_2O contents in magma (Loucks 2014).

On the An vs. Al/(Ca+Na+K) diagram (Williamson et al. 2016), most samples from the northern and southern intrusions plot within the barren field. Fig 8g shows higher Al content and magmatic water for the northern intrusion than the southern gabbro-diorite. Two samples from the northern intrusion plot in a fertile area and the other plots near the fertile area. The minor metal contents in magnetite minerals from the northern intrusion are widely spread across the compositional fields for porphyry mineralization (Fig 8h).

Biotites from barren and mineralized intrusions show contrasting major element geochemistry. Analyzed crystals from barren intrusions are classified as magnesian siderophyllite, whereas the ones from the Cu-Mo systems are considered ferroan phlogopite and those from Sn-W-Mo systems as lithian siderophyllite in accord with the International Mineralogical Association (IMA) classification diagram (Rieder et al. 1998). The EPMA results show that biotite minerals from the northern intrusion are classified as ferroan phlogopite (Table 2c). Based on all obtained data, the studied magmas originated from a mixed mantle-crust melting and are associated with a subduction-related environment. Therefore, one of the reasons for the fertility of the northern intrusions and the infertility of the southern intrusions could probably be due to their locations relative to the subduction zone and magma source materials (Fig 9). These led to higher H_2O contents in magma.

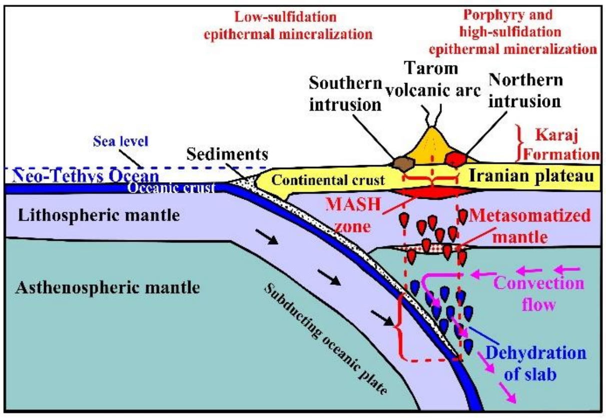

Fig 9. The schematic cross-section for the formation of northern and southern intrusions in the Tarom metallogenic belt.

7. Conclusions

Petrographic study and mineral chemistry by EPMA revealed that the Tarom northern and southern intrusions show calc-alkaline characteristics and are emplaced within an arc-related tectonic environment. The Tarom northern intrusion: Plagioclases have an An_{22} to An_{49} composition (oligoclase to labradorite). Biotite minerals are Mg- and Fe-rich and ferroan phlogopite. Biotite composition and magnetite occurrence confirm the high oxygen fugacity of the magma. The biotite crystals crystallized at high temperatures. The pyroxene crystallized at <2 to 5*kbar* and $H_2O=10\%$. The crystallization temperature of pyroxene is 1100-1175°*C*. The feldspars temperatures are ~550°*C*. The mineral composition of pyroxene, plagioclase, and biotite implies that the parental magma was fertile for porphyry mineralization. The northern quartz monzonite was sourced from the melting of a mixed mantle-crust source in a subduction-related environment.

The Tarom southern intrusion: Plagioclases from the southern intrusion series and gabbro-diorite shows An_{35} to An_{54} (andesine to labradorite) and An_{56} to An_{61} (labradorite) composition, respectively. The pyroxenes crystallized at an $H_2O=10\%$. The crystallization pressure of clinopyroxene in the southern intrusions starts from <2 to 5*kbar*. The crystallization temperature of clinopyroxene is 1140-1185°*C*. Feldspars indicate a temperature range of 550 to 600°*C*. The southern intrusion emplaced in a subduction-related setting. The crystallization conditions suggest that the Tarom northern and southern intrusions formed at high temperatures, shallow depths, and under very high oxygen fugacity conditions. The coexistence of plagioclase with amphibole and biotite phenocrysts shows that the original magma of the magmatic rocks had higher than 1.5*wt.%* H_2O content (Thorpes 1982). These results suggest that the northern and southern intrusions have the potential for future mineral exploration similar to what has already been identified at the Chodarchay Cu deposit in the northern quartz monzonite and mineralization inside the Chargar gabbro-diorite. Of course, the mineral chemistry of the northern intrusion shows characteristics of porphyry formation, but the southern intrusion does not show such features. This fertility difference between the northern and southern intrusions can be due to the location of these intrusions relative to the subduction zone and their magma source materials. The northern intrusion is younger than the southern one and is probably related to the post-collision stage. Its magma crystallized at a lower pressure.

Acknowledgments

This paper is part of the first and third authors' Ph.D. thesis projects at Tarbiat Modares University, Tehran, Iran. We would like to thank the financial support from both Tarbiat Modares University and the Iranian Mines and Mining Industries Development and Renovation Organization (IMIDRO).

References

Abdel Rahman AM (1994) Nature of biotites from alkaline, calc-alkaline and peraluminous magmas, *Journal of Petroleum Science and Technology* 35: 525–541.

Anderson J L (1996) Status of thermobarometry in granitic batholiths, *Transactions of the Royal Society of Edinburgh* 87: 125–138.

Annells RN, Arthurton RS, Bazely RA, Davis RG (1975) Explanatory text of the Qazvin and Rasht quadrangles map (1:250000). Geological Survey of Iran.

Aoki K, Shiba I (1973) Pyroxenes from lherzolite inclusions of Itinomegata-Gata, Japan, *Lithos* 6: 41–51.

Asiabanha A, Foden J (2012) Post-collisional transition from an extensional volcano-sedimentary basin to a continental arc in the Alborz ranges, N-Iran, *Lithos* 148: 98–111.

Axen GJ, Lam PJ, Grove M, Stockli DF, Hassanzadeh J (2001) Exhumation of the west-central Alborz Mountains, Iran, Caspian subsidence, and collision-related tectonics, *Geology* 29: 559–562.

Barbarian B (1990) Granitoids: Main petrogenetic classifications in relation to origin and tectonic setting, *Geological Journal* 25: 227–238.

Beane RE (1974) Biotite stability in the porphyry copper environment, *Economic Geology* 69: 241–256.

Beccaluva L, Macciotta G, Piccardo GB, Zeda O (1989) Clinopyroxene composition of ophiolite basalts as petrogenetic indicator, *Chemical Geology* 77: 165–182.

Bindi L, Cellai D, Melluso L, Conticelli S, Morra V et al. (1999) Crystal chemistry of clinopyroxene from alkaline undersaturated rocks of the Monte Vulture volcano, Italy, *Lithos* 46: 259–274.

Botcharnikov R, Koepke J, Holtz F, Mc Cammon C, Wlike M (2005) The effect of water activity on the oxidation and structural state of Fe in a ferro-basaltic melt, *Geochimica et Cosmochimica Acta* 69: 5071–5085.

Castro A, Aghazadeh M, Badrzadeh Z, Chichorro M (2013) Late Eocene–Oligocene post-collisional monzonitic intrusions from the Alborz magmatic belt, NW Iran: An example of monzonite magma generation from a metasomatized mantle source, *Lithos* 180-181: 109–127.

Castro A, Stephen WE (1992) Amphibole rich clots in calc-alkaline granitic rocks and their enclaves, *The Canadian Mineralogist* 30: 1093–1112.

Cooke DR, Agnew P, Hollings P, Baker M, Chang Z et al. (2017) Porphyry indicator minerals (PIMS) and porphyry vectoring and fertility tools (PVFTS) – Indicators of mineralization styles and recorders of hypogene geochemical dispersion halos. In: Proceedings of Exploration 17, Sixth Decennial International Conference on Mineral Exploration, V. Tschirhart and M.D. Thomas, eds., *Geochemistry* 457–469.

Dabovski C, Harkovska A, Kamenov B, Mavrudchiev B, Stanisheva-Vassileva G et al. (1991) A geodynamic model of the Alpine magmatism in Bulgaria, *Geologica Balcanica* 21: 3–15.

Deer WA, Howie RA, Zussman J (1992) An introduction to the rock-forming minerals. 17th ed., Longman, London.

Deol S, Deb M, Large RR, Gilbert S (2012) LA-ICPMS and EPMA studies of pyrite, arsenopyrite and loellingite from the Bhukia-Jagpura gold prospect, southern Rajasthan, India: Implications for ore genesis and gold remobilization, *Chemical Geology* 326: 72–87.

Dupuis C, Beaudoin G (2011) Discriminant diagrams for iron oxide trace element fingerprinting of mineral deposit types, *Mineralium Deposita* 46: 319–335.

France L, Koepke J, Ildefonse B, Cichy SB, Deschamps F (2010) Hydrous partial melting in the sheeted dike complex at fast-spreading ridges: Experimental and natural observations, *Contributions to Mineralogy and Petrology* 160: 683–704.

Green DH, Ringwood AE (1967) An experimental investigation of the gabbro to eclogite transformation and its petrological applications, *Geochimica et Cosmochimica Acta* 31: 767–833.

Helgadottir H (2016) Comparative analysis of plagioclase in the Eyjafjöllankaramites, BSc thesis, Faculty of Earth Science, School of Engineering and Natural Sciences, University of Iceland, 67.

Helz RT (1976) Phase relations of basalts in their melting ranges at PH_2O= 5kb as a function of oxygen fugacity, part I. Mafic phases, *Journal of Petroleum Science and Engineering* 14: 249–302.

Hirayama K, Haghipour A, Hajian J (1965) Geology of the Zanjan area: The Tarom district, eastern part (Zanjan area, northwest Iran), with a 1: 100,000 map. Geological Survey of Iran, Tehran 28: 33 p.

Hirayama K, Samimi M, Zahedi M, Hushmand-Zadeh A (1966) Geology of Taroum district, western part (Zanjan area north-west Iran), Geological Survey of Iran.

Hosseini M, Moosavi E, Rasouli Jamadi F (2017) Abhar 1: 100000 Geological map, Geological Survey of Iran.

Hout F, Hebert R, Varfalvy V, Beaudin G, Wang CS, et al. (2002) The Beimarang Mélange (southern Tibet) brings additional constraints in assessing the origin, metamorphic evolution and obduction processes of the Yarlung Zangbo ophiolite, *Journal of Asian Earth Sciences* 21: 307–322.

Kilinc A, Carmichael I, Rivers M, Sack R (1983) The ferric-ferrous ratio of natural silicate liquids equilibrated in air, *Contributions to Mineralogy and Petrology* 83: 136–140.

Kroll H, Evangelakis C, Voll G (1993) Two-feldspar geothermometry: a review and revision for slowly cooled rocks, *Contributions to Mineralogy and Petrology* 114: 510–518.

Kretz R (1983) Symbols for rock-forming minerals, *American Mineralogist* 68: 277–279.

Kushiro I (1960) Si-Al relation in clinopyroxenes from igneous rocks, *American Journal of Science* 258: 548–554.

Le Bas NJ (1962) The role of aluminum in igneous pyroxenes with relation to their parentage, *American Journal of Science* 260: 267–288.

Leterrier J, Maurry RC, Thonon P, Girard D, Marchal M (1982) Clinopyroxene composition as a method of identification of the magmatic affinities of paleo-volcanic series, *Earth and Planetary Science Letters* 59: 139–154.

Loucks RR (2014) Distinctive composition of copper-ore forming arc magmas, *Australian Journal of Earth Sciences* 61: 5–16.

Moinvaziri H (1985) Volcanismet ertiaire et quaternaire en Iran. Université Paris-Sud, Orsay, These d'Etat, 278.

Molina J, Scarrow J, Montero PG, Bea F (2009) High-Ti amphibole as a petrogenetic indicator of magma chemistry: Evidence for mildly alkalic-hybrid melts during evolution of Variscan basic-ultrabasic magmatism of Central Iberia, *Contributions to Mineralogy and Petrology* 158: 69–98.

Moretti R (2005) Polymerisation, basicity, oxidation state and their role in ionic modeling of silicate melts, *Annales Geophysicae* 56: 340–368.

Morimoto N, Fabries J, Ferguson AK, et al. (1988) Nomenclature of Pyroxenes. *Mineralogical Magazine* 52: 535–550.

Mousavi Motlagh SH, Ghaderi M (2019) The Chargar Au-Cu deposit: An example of low-sulfidation epithermal mineralization from the Tarom subzone, NW Iran, *Neues Jahrbuch für Mineralogie, Abhandlungen* 196(1): 43–66.

Mousavi Motlagh SH, Ghaderi M, Mokhtari MAA, Yasami N (2019) Geochemical constraints on the origin and tectonic setting of Chargar intrusions in the Alborz orogenic belt, NW Iran, *Journal of Earth System Science* 128: 224.

Nabatian Gh, Jiang SY, Honarmand M, Neubauer F (2016) Zircon U–Pb ages, geochemical and Sr–Nd–Pb–Hf isotopic constraints on petrogenesis of the Tarom-Olya pluton, Alborz magmatic belt, NW Iran, *Lithos* 244: 43–58.

Nachit H, Ibhi A, Abia EH, Ohoud MB (2005) Discrimination between primary magmatic biotites, reequilibrated biotites and neoformed biotites, *Comptes Rendus Geoscience* 337: 1415–1420.

Nisbet EG, Pearce JA (1977) Clinopyroxene composition of mafic lavas from different tectonic settings, *Contributions to Mineralogy and Petrology* 63(2): 161–173.

Nazari H, Salamati R (1998) 1:100,000 scale geological map of the Roudbar quadrangle. *Geological Survey of Iran.*

Perarce JA, Harris NB, Tindle AG (1984) Trace element discrimination diagrams for the tectonic interpretation of granitic rocks, *Journal of Petroleum Science and Technology* 25: 956–983.

Piccoli PM, Candela PA (2002) Apatite in igneous systems, *Reviews in Mineralogy and Geochemistry* 48: 255–292.

Richards JP (2016) Tectonics and Metallogeny of the Tethyan Orogenic Belt. *Society of Economic Geologists* 19.

Ricou LE, Burg JP, Godfriaux I, Ivanov Z (1998) Rhodope and Vardar: The metamorphic and the olistostromic paired belts related to the Cretaceous subduction under Europe, *Acta Geodynamica et Geomaterialia* 11(6): 285–309.

Rieder M, Cavazzini G, D'yakonov YS, Frank-Kamenetskii VA, Gottardi G, et al. (1998) Nomenclature of the micas, *Clay Minerals* 46: 586–595.

Rolland Y, Billo S, Corsini M, Sosson M, Galyan G (2009) Blueschists of the Amassia-Stepanavan suture zone (Armenia): Linking Tethys subduction history from E-Turkey to W-Iran, *International Journal of Earth Sciences* 98: 533–550.

Sarem MN, Abedini MV, Dabiri R, Ansari MR (2021) Geochemistry and Petrogenesis of Basic Paleogene Volcanic Rocks in Alamut Region. *Earth Sciences Research Journal* 25(2):237-45.

Schweitzer E, Papike J, Bence A (1979) Statistical analysis of clinopyroxenes from deep-sea basalts, *American Mineralogist* 64: 501–513.

Seck HA (1971) Koexistierende alkali feldspateundplagioklaseim system $NaAlSi_3O_8$-$KAlSi_3O_8$-$CaAl_2Si_2O_8$-H_2O beitemperaturen von 650°C bis 900°C, *Neues Jahrbuch für Mineralogie, Abhandlungen* 115: 315–345.

Seedorff E, Dilles JH, Proffett JMJr, Einaudi L, Zurcher WJA, et al. (2005) Porphyry deposits: Characteristics and origin of hypogene features, *Economic Geology* 100: 251–298.

Soesoo A (1997) A multivariate statistical analysis of clinopyroxene composition: Empirical coordinates for the crystallisation PT-estimations. *Geological Society of Sweden (Geologiska Föreningen)* 119(1): 55–60.

Streckeisen A (1976) To each plutonic rock its proper name, *Earth-Science Review* 12: 1–33.

Streckeisen A, Le Maitre RW (1979) A chemical approximation to the modal QAPF classification of the igneous rocks, *Neues Jahrbuch für Mineralogie, Abhandlungen* 136: 169–206.

Sun WD, Arculus RJ, Kamenetsky VS, Binns RA (2004) Release of gold-bearing fluids in convergent margin magmas prompted by magnetite crystallization, *Nature* 431: 975–978.

Taylor W, Nimis J (2000) Thermometry clinopyroxene in the Hawaii basalt, *Mineralogy* 21: 25–36.

Thorpes RS (ed) (1982) Andesites. Wiley, Chichester, 724.

Williamson BJ, Herrington RJ, Morris A (2016) Porphyry copper enrichment linked to excess aluminum in plagioclase, *Nature Geoscience* 9: 237–242.

Wones DR, Eugster HP (1965) Stability of biotite: Experiment, theory and application, *American Mineralogist* 50: 1228–1272.

Wyborn D, Sun SS (1994) Sulphur-undersaturated magmatism: A key factor for generating magma-related copper-gold deposits. AGSO Research Newsletter 21: 7–8.

Yasami N (2018) Geology, alteration, geochemistry and genesis of Chodarchay Cu deposit, Tarom subzone, east Zanjan, Ph.D. thesis, Tarbiat Modares University, Iran.

Yasami N, Ghaderi M, Madanipour S, Taghilou B (2017) Structural control on overprinting high-sulfidation epithermal on porphyry mineralization in the

Chodarchay deposit, northwestern Iran, *Ore Geology Reviews* 86: 212–224.

Yasami N, Ghaderi M, Mokhtari MAA, Mousavi Motlagh SH (2018) Petrogenesis of the two phases of intrusive rocks at Chodarchay, NW Iran: Using trace and rare earth elements, NW Iran, *Arabian Journal of Geosciences* 11(20): 605.

Zamanian H, Rahmani Sh, Zareisahamieh R (2019) Fluid inclusion and stable isotope study of the Lubin-Zardeh epithermal Cu-Au deposit in Zanjan Province, NW Iran: Implications for ore genesis, *Ore Geology Reviews* 112: 103014.

Yazdi A, Ashja Ardalan A, Emami MH, Dabiri R, Foudazi M. (2019) Magmatic interactions as recorded in plagioclase phenocrysts of quaternary volcanics in SE Bam (SE Iran). *Iranian Journal of Earth Sciences*11(3):215-25.

Zhou ZX (1986) The origin of intrusive mass in Fengshandong, Hubei province, *Acta Petrologica Sinica* 2(1): 59–70.